ACS APPLIED POLYMER MATERIALS

Open Access
This article is licensed under CC-BY 4.0

pubs.acs.org/acsapm
Article

Thianthrene- and Thianthrene Tetraoxide-Functionalized Conjugated Microporous Polymers for Efficient Energy Storage

Abdul Basit,[⊥] Mohamed Gamal Mohamed,[⊥] Santosh U. Sharma, and Shiao-Wei Kuo*

Cite This: ACS Appl. Polym. Mater. 2024, 6, 12247−12260
Read Online

ACCESS | Metrics & More | Article Recommendations | Supporting Information

ABSTRACT: Supercapacitors (SCs), with their exceptional properties, present a promising solution to the ongoing energy crisis by meeting the increasing demand for high-energy storage devices. Conjugated microporous polymers (CMPs) offer a range of sizes, precisely controlled porosities, impressive intrinsic porosity, remarkable stability, and customizable structures and functionalities. These attributes collectively make CMPs cost-effective materials for energy storage applications. In this research, we effectively created three organic electrodes based on CMPs for energy storage via the Suzuki coupling reaction of 1,3,6,8-tetrakis(4-bromophenyl)pyrene (PyPh-Br_4) and benzene-1,4-diboronic acid (BZ-2B$(OH)_2$) with 2,8-dibromothianthrene (Th-Br_2) or 3,7-dibromodibenzothiophene *S*, *S*-dioxide (SU-Br_2) or 2,8-dibromothianthrene-5,5′,10,10′-tetraoxide (DSU-Br_2) to produce PyPh-BZ-Th, PyPh-BZ-SU, and PyPh-BZ-DSU CMP, respectively. Their thermal stability was examined using TGA measurements, and both PyPh-BZ-Th CMP and PyPh-BZ-SU CMP displayed T_{d10} of 540 and 467 °C with high carbon reside up to 70 wt % at 800 °C. Electrochemical performance for these materials was evaluated using cyclic voltammetry (CV) and galvanostatic charge−discharge (GCD). Within a three-electrode setup, specific capacitances of 617, 538, and 596 F g^{-1} for PyPh-BZ-Th, PyPh-BZ-SU, and PyPh-BZ-DSU CMPs were recorded by GCD at 0.5 A g^{-1}. To obtain a more practical and accurate evaluation, we further constructed symmetric devices for each CMP. Using GCD curves, the specific capacitances were found to be 187, 63, and 105 F g^{-1}, respectively, for PyPh-BZ-Th, PyPh-BZ-SU, and PyPh-BZ-DSU CMPs. The high capacitances of the synthesized CMPs in this study, comparable to those of other reported porous CMPs, can be attributed to electronegative moieties, such as sulfur (S) and sulfone (SO_2) groups. These groups enhance electrostatic interactions and improve the wettability of the electrodes. This study demonstrates that using the Suzuki coupling reaction technique, CMPs incorporating Py, Th, and DSU moieties can be effectively produced for energy storage applications.

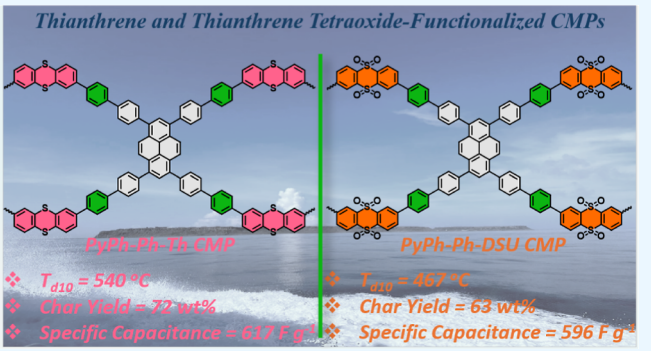

KEYWORDS: *thianthrene, thianthrene-5,5′,10,10′-tetraoxide, conjugated microporous polymers, thermal stability, supercapacitors*

Downloaded via NATL SUN YAT-SEN UNIV on February 17, 2025 at 08:48:04 (UTC).
See https://pubs.acs.org/sharingguidelines for options on how to legitimately share published articles.

INTRODUCTION

Increasing concerns about energy shortages and resource depletion, which present significant environmental risks, have intensified the emphasis on creating efficient and environmentally friendly energy storage systems (ESSs).[1−9] The depletion of natural resources has intensified the quest for alternative energy sources that offer high energy and power density, prolonged cycle life, excellent reversibility, and efficient energy storage.[10−15] Electrochemical techniques have become indispensable in addressing these energy crises within energy storage technology.[16−20] The emergence of innovative storage technologies, including supercapacitors (SCs) and high-capacity batteries with elevated specific power and energy storage capabilities, has become a significant focal point in both academic research and industrial sectors.[21,22] In the realm of ESSs, SCs have gained increasing attention due to their remarkable stability across temperature ranges, exceptional cycling capabilities, ease of production, and impressive energy and power densities.[23−26]

SCs store charge through two distinct mechanisms: electrostatic and faradaic. The electrostatic mechanism, known as electric double-layer capacitance (EDLC), involves storing charges at the interface of the SC electrode. In contrast, the faradaic mechanism or pseudocapacitance (PC), involves storing charges at the electrode surface through highly reversible surface redox reactions during charge and discharge processes.[27−30] The EDLC of materials is closely linked to the surface areas. Materials with large surface areas, such as

Received: July 28, 2024
Revised: September 18, 2024
Accepted: September 23, 2024
Published: October 1, 2024

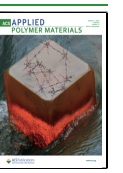

© 2024 The Authors. Published by American Chemical Society

carbonaceous materials and CMPs, typically exhibit high EDLC behaviors.[31−35] Therefore, it is crucial to investigate novel electrode materials that effectively combine both EDLC and PC mechanisms. An optimal electrode material should possess specific attributes, including ideal redox-active sites, high-specific surface area (SSA), excellent conductivity, appropriate pore width, robust chemical and thermal stability, and environmental friendliness.[36]

Porous materials have found extensive applications across various technological and scientific domains, leading to the development of numerous advanced variants over the past 20 years.[37−42] During this period, research groups have synthesized various subclasses of porous organic polymer (POP) frameworks, including covalent triazine frameworks (CTFs), COFs, hyper-cross-linked polymers (HCPs), porous aromatic frameworks (PAFs), and CMPs.[43−46] Among all of these, CMPs offer numerous advantageous characteristics, such as optoelectronic properties, high surface area, straightforward synthesis, heightened responsiveness to visible light, and exceptional thermal stability.[36,42] CMPs, known for their enduring microporous structure and extensive π-conjugated framework, were first identified in 2007. These materials have since emerged as a significant subgroup within porous materials due to the diversity of synthetic building blocks and accessible network-forming techniques. This variety has led to the development of numerous CMPs, each with unique structures and characteristics.[36,42] Consequently, CMPs have been tailored for applications in biological uses, sensing, light emission, chemical adsorption, gas adsorption and separation, encapsulation, energy storage, and solar fuel production.[36,42,47−53] In addition to these characteristics, CMPs can be made in a variety of architectures, including 2-D and 3-D networks, dendrimers, and branched polymers. A crucial aspect of CMPs is their ability to precisely control pore size, chemical composition, and overall structure.[36,42]

The pyrene (Py) moiety exhibits an extended π-conjugation and a planar configuration. These features are typical of a donor. CMPs based on Py moieties have been synthesized for various applications, including energy storage and optoelectronic devices.[50,54] Thianthrene (Th) is an aromatic sulfur-containing heterocyclic compound that has gained significant attention in various fields of chemistry due to its unique structural and electronic properties.[30,55,56] The molecule consists of two benzene rings fused to a central sulfur (S) atom, forming a planar structure with an extended π-conjugation. This configuration imparts Th with notable thermal stability, electron-donating characteristics, and the ability to interact with $\pi-\pi$ stacking.[30,55,56] Th and its derivatives have been extensively researched for organic electronics, photovoltaics, and catalysis applications. Its conjugated structure and sulfur content make Th a substance that shows promise for creating sophisticated electrodes for energy storage, particularly in lithium−sulfur (Li−S) batteries and SCs.[30,55,56] Incorporating Th and its derivative moieties into CMPs can enhance their electrochemical performance by improving surface area, conductivity, and electrochemical stability. For example, research by Mohamed et al. highlighted that using an acetylene bridge in P−Th−POP led to a specific capacitance of 217 F g^{-1} (at 0.5 A g^{-1}).[30] In another instance, CMPs based on TPE-Ph-BSu demonstrated considerable energy storage capacity, achieving 52 F g^{-1}.[57] Furthermore, the CMP electrode incorporating TBN-BSU registered a capacitance of 70 F g^{-1}.[58] Li et al. reported the TAT-CMP-1 and TAT-CMP-2 with capacitance of 141 and 183 F g^{-1} for SC applications.[59] However, Wang et al. reported the composite of CMP with MWCNT with the specific capacitance of 248 F g^{-1}.[60]

To address the concerns mentioned above, we synthesized PyPh-BZ-Th, PyPh-BZ-SU, and PyPh-BZ-DSU CMPs through Suzuki polymerization of PyPh-Br_4 and BZ-2B$(OH)_2$ in the presence of a Pd$(PPh_3)_4$ catalyst, utilizing Th-Br_2, SU-Br_2, or DSU-Br_2. We employed a range of spectroscopic and microscopic methods to conduct thorough analyses of the thermal decomposition temperatures, molecular architectures, texture, and porosity of these CMPs. When investigating their thermal stability using TGA measurements, we found that PyPh-BZ-Th and PyPh-BZ-SU CMPs exhibited T_{d10} values of 467 and 540 °C, respectively, with high char yield reaching 70 wt % at 800 °C. Additionally, we conducted electrochemical measurements, including both three-electrode and symmetric coin cell configurations, to determine the potential of these CMPs for use in energy storage, we conducted galvanostatic charge−discharge (GCD) tests. For the PyPh-BZ-Th, PyPh-BZ-SU, and PyPh-BZ-DSU CMPs, specific capacitances measured at 0.5 A g^{-1} in a three-electrode setup were 617, 538, and 596 F g^{-1}, respectively. When tested in symmetric SC coin cells at 1 A g^{-1}, the specific capacitances recorded were 187, 63, and 105 F g^{-1} for PyPh-BZ-Th, PyPh-BZ-SU, and PyPh-BZ-DSU CMPs, respectively.

EXPERIMENTAL SECTION

Materials. Dibenzo[*b*,*d*]thiophene sulfone (SU, 97%), nitrobenzene (99%), hydrogen peroxide (H_2O_2), benzene-1,4-diboronic acid (BZ-2B$(OH)_2$, 95%), Py (98%), *N*-bromosuccinimide (NBS, 99%), 4-bromophenylboronic acid (PhB$(OH)_2$-Br, 95%), Th (97%), tetrahydrofuran (THF), potassium carbonate (K_2CO_3, 99.8%), bromine solution (Br_2), acetic acid (AcOH), 1,4-dioxane (DO), acetone, tetrakis(triphenylphosphine)palladium [Pd$(PPh_3)_4$, 98%], sulfuric acid (H_2SO_4), and anhydrous magnesium sulfate ($MgSO_4$, 99.5%), were obtained from Sigma-Aldrich and Alfa Aesar.

Synthesis of PyPh-Br_4. Under vacuum, a mixture was prepared including Pd$(PPh_3)_4$ (0.8 g, 0.68 mmol), PhB$(OH)_2$-Br (3.3 g, 22 mmol), K_2CO_3 (4.3 g, 30.8 mmol), and Py-Br[61−65] (2 g, 3.8 mmol) in a solution of DO/H_2O [100 mL/40 mL]. This mixture was subjected to heating for 48 h at 110 °C under N_2. After the reaction, the solution underwent a filtration process, and the yellow powder was washed using H_2O, THF, and MeOH [Scheme S1]. FTIR: 3037.11 (C/H aromatic), 1592.24 cm^{-1} [Figure S1]. HR-FD-MS [Figure S2]: *m*/*z*: 822.90.

Synthesis of Th-Br_2. Br_2 (13 mL), Th (7 g, 32.41 mmol), and AcOH (130 mL) were successively added to a 100 mL round-bottom flask. The contents were then heated to 90−95 °C and maintained at this temperature for 16 h. Following the heating period, 60 mL of DI water was included in the mixture to cause a white solid to precipitate. This solid, identified as Th-Br_2, was purified through recrystallization with MeOH/DCM to obtain Th-Z-Br_2 (6.2 g, Scheme S2). FTIR: 3057.72, 1540.86, and 1436.64 cm^{-1} [Figure S3]. ^{1}H NMR: 7.72, 7.63, and 7.33 ppm [Figure S4]. ^{13}C NMR: 138−122.45 ppm [Figure S5].

Synthesis of SU-Br_2. To dissolve 6 g (28 mmol) of SU, 195 mL of H_2SO_4 was used at 0 °C. NBS (9.91 g, 56 mmol) was then gradually added in portions, and the mixture was stirred for 10 h at 25 °C. Subsequently, the mixture was carefully added to cooled water, extracted with $CHCl_3$, dried over $MgSO_4$, and concentrated by using a rotary evaporator. The resulting crude product was purified by column chromatography with a hexane/DCM (1:1) mixture, yielding 8 g of SU-Br_2 as a white powder [Scheme S3]. FTIR (Figure S6): 3083.11, 1302.78, and 1168.72 (SO_2) cm^{-1}. ^{1}H NMR (Figure S7): 8.36, 8.15, and 8.03 ppm. ^{13}C NMR (Figure S8): 139.1−124.89 ppm.

https://doi.org/10.1021/acsapm.4c02368
ACS Appl. Polym. Mater. 2024, 6, 12247−12260

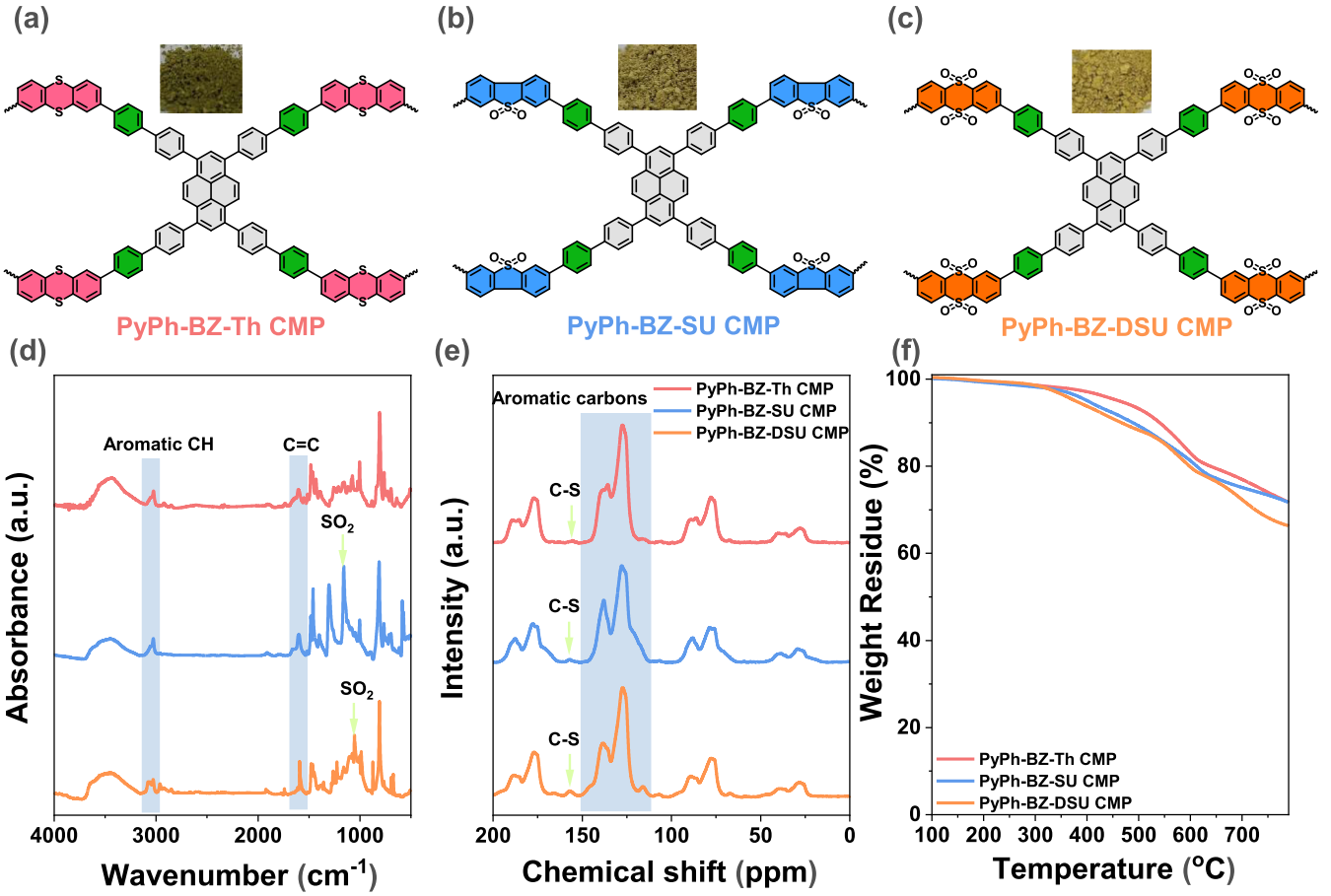

Figure 1. (a–c) Molecular configurations, (d) FTIR spectra, (e) solid-state ^{13}C NMR data, and (f) TGA of PyPh-BZ-Th CMP, PyPh-BZ-SU CMP, and PyPh-BZ-DSU CMP.

Synthesis of DSU-Br$_2$. Th-Br$_2$ (4 g, 11 mol) was dissolved in AcOH (87 mL), followed by the gradual addition of H_2O_2 (110 mL). The solution was then stirred and heated to 90–95 °C for 1 day. The precipitate was filtered and rigorously washed with water and $NaHCO_3$ solution once it had cooled to room temperature. The DSU-Br$_2$ product was further purified by recrystallization using a mixture of MeOH/DCM, yielding a white solid, DSU-Br$_2$ [Scheme S4]. FTIR [Figure S9]: 3061.72, 1558.91, 1331.78, and 1167.44 (SO_2 group) cm^{-1}. ^1H NMR (ppm, Figure S10): 8.5 (2H), 8.3 (2H), 7.98 (2H); ^{13}C NMR (ppm): 139.21–129.41.

Preparation of PyPh-BZ-Th CMP, PyPh-BZ-SU CMP, and PyPh-BZ-DSU CMP. In a 25 mL Schlenk tube was placed a mixture of Pd(PPh$_3$)$_4$ (0.03 g), PyPh-Br$_4$ (2 mmol), BZ-2B(OH)$_2$ (4 mmol), 2 M K_2CO_3 (10 mL), and either Th-Br$_2$, SU-Br$_2$, or DSU-Br$_2$ (1 mmol) into DMF (35 mL). Reflux the solution at 110 °C for 3 days. Following this, the solid should be filtered and purified through Soxhlet extraction using THF followed by MeOH. This procedure results in the formation of PyPh-BZ-Th CMP as a dark green solid [yield: 70%, Scheme S5], PyPh-BZ-SU CMP as a light green solid [yield: 80%, Scheme S6], and PyPh-BZ-DSU CMP as a yellow powder [yield: 85%, Scheme S7].

RESULTS AND DISCUSSION

Characterization of PyPh-BZ-Th CMP, PyPh-BZ-SU CMP, and PyPh-BZ-DSU CMP. This work explores the construction of CMPs tethered with Py, Th, dibromodibenzothiophene *S*,*S*-dioxide, and thianthrene-5,5′,10,10′-tetraoxide for efficient energy storage. By leveraging the unique properties of Th, the synthesized CMPs are expected to exhibit superior performance in terms of capacitance, charge–discharge efficiency, and overall energy storage capacity. We synthesized three CMPs, named PyPh-BZ-Th CMP, PyPh-BZ-SU CMP, and PyPh-BZ-DSU CMP for SC applications using a Suzuki reaction. The synthesis involved the reaction of PyPh-Br$_4$ with Th-Br$_2$, SU-Br$_2$, or DSU-Br$_2$ in the presence of BZ-2B(OH)$_2$, 2 M K_2CO_3, and Pd(PPh$_3$)$_4$, at 110 °C for 72 h in DMF solution to afford PyPh-BZ-Th CMP as a dark green solid, PyPh-BZ-SU CMP as a light green solid, and PyPh-BZ-DSU CMP as a yellow powder, as indicated in Figure 1a–c and Schemes S5–S7. The resultant CMPs exhibited minimal solubility in organic solvents, confirming the formation of a conjugated cross-linked network. The precursors PyPh-Br$_4$, Th-Br$_2$, SU-Br$_2$, and DSU-Br$_2$ were effectively synthesized with high efficiency. PyPh-Br$_4$ was produced as a yellow solid via Suzuki coupling between Py-Br$_4$ and PhB(OH)$_2$-Br. Th-Br$_2$ was obtained as a white solid by reacting Br$_2$ with Th in the presence of AcOH. Dibenzo[*b*,*d*]thiophene sulfone, known as SU, was generated by reacting NBS with H_2SO_4 to form the white solid SU-Br$_2$. Finally, DSU-Br$_2$ was successfully produced through the reaction of Th-Br$_2$ with a mixture of H_2O_2 and acetic acid. FTIR and NMR spectral analyses, as detailed in the Experimental Section and Supporting Information, confirmed the successful synthesis of all monomers used in this work [Figures S1–S10]. The FTIR spectra (Figure 1d) of all CMPs display peaks in the ranges 3030–3038 and 1599–1614 cm^{-1}, which correspond to aromatic CH and C=C bonds, respectively. Additional peaks between 1167 and 1168 and 1331–1302 cm^{-1} are observed in the spectra of PyPh-BZ-SU

https://doi.org/10.1021/acsapm.4c02368
ACS Appl. Polym. Mater. 2024, 6, 12247–12260

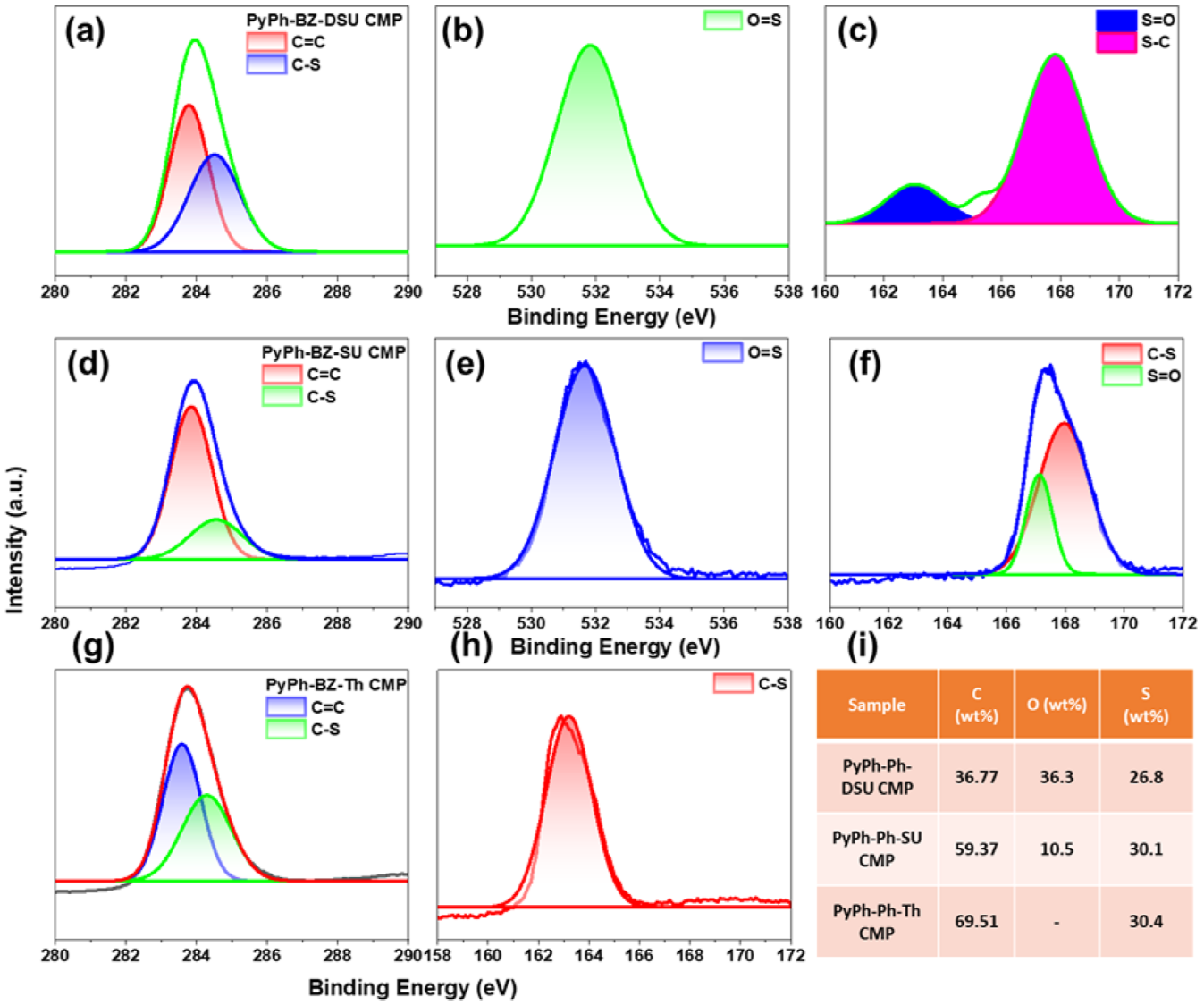

Sample	C (wt%)	O (wt%)	S (wt%)
PyPh-Ph-DSU CMP	36.77	36.3	26.8
PyPh-Ph-SU CMP	59.37	10.5	30.1
PyPh-Ph-Th CMP	69.51	-	30.4

Figure 2. (a–h) XPS fitting results and (i) elemental composition by weight percentage for C, O, and S in the frameworks of PyPh-BZ-Th, PyPh-BZ-SU, and PyPh-BZ-DSU CMPs.

CMP and PyPh-BZ-DSU CMP, indicating SO_2 stretching vibrations.[57,58,66] These peaks are not present in the PyPh-BZ-Th CMP spectrum. Solid-state CPMAS ^{13}C NMR analysis (Figure 1e) shows characteristic peaks for aromatic C=C bonds ranging from 139.45 to 127.40 ppm in PyPh-BZ-Th CMP. Similarly, PyPh-BZ-SU CMP exhibits peaks between 138.62 and 118.79 ppm, while PyPh-BZ-DSU CMP shows peaks from 138.45 to 127.48 ppm. Additionally, signals at 155.95, 156.38, and 156.38 ppm in the ^{13}C NMR spectra of PyPh-BZ-Th CMP, PyPh-BZ-SU CMP, and PyPh-BZ-DSU CMP, respectively, are attributed to the C–S bond in their structures.[30,66] Furthermore, thermogravimetric analysis (TGA) was used to examine the decomposition behavior of PyPh-BZ-Th, PyPh-BZ-SU, and PyPh-BZ-DSU CMPs (Figure 1f). The percentage of carbon residue for PyPh-BZ-Th CMP was 72 wt % at a T_{d10} value of 540 °C. For PyPh-BZ-SU CMP and PyPh-BZ-DSU CMP, the carbon residue percentages were 71 and 63 wt %, with T_{d10} values of 489 and 467 °C, respectively.

In addition to this, we also employed X-ray photoelectron spectroscopy (XPS) to confirm the presence of C, S, and O in the CMPs (Figure 2a–h). XPS provides valuable insights into the surface composition, chemical states of elements, and interactions at the polymer surface. The signal corresponding to C=C at 283.5, 238.8, and 283.7 eV correlates to PyPh-BZ-Th CMP, PyPh-BZ-SU CMP, and PyPh-BZ-DSU CMP, respectively. The signals at 284.3, 284.6, and 284.4 eV correspond to C–S for PyPh-BZ-Th CMP, PyPh-BZ-SU CMP, and PyPh-BZ-DSU CMP, respectively. The signals at 531.6 and 531.7 eV for O=S in PyPh-BZ-SU CMP and PyPh-BZ-DSU CMP, respectively, confirm the presence of oxygen in these structures, while its absence in PyPh-BZ-Th-CMP confirms the absence of oxygen. The signals at 163.7, 167.7, and 167.8 eV correspond to C–S for PyPh-BZ-Th CMP, PyPh-BZ-SU CMP, and PyPh-BZ-DSU CMP, respectively. The presence of S=O shifts the C–S signal to 167 eV in PyPh-BZ-SU CMP and PyPh-BZ-DSU CMP, whereas it gives a signal at 163.7 eV for PyPh-BZ-Th CMP. The corresponding signal at 167 and 163 eV relates to S=O for PyPh-BZ-SU CMP and PyPh-BZ-DSU CMP, respectively. The weight percentages [Figure 2i] for C, O, and S in the PyPh-BZ-SU and PyPh-BZ-DSU CMPs were determined to be 36.77, 36.3,

https://doi.org/10.1021/acsapm.4c02368
ACS Appl. Polym. Mater. 2024, 6, 12247–12260

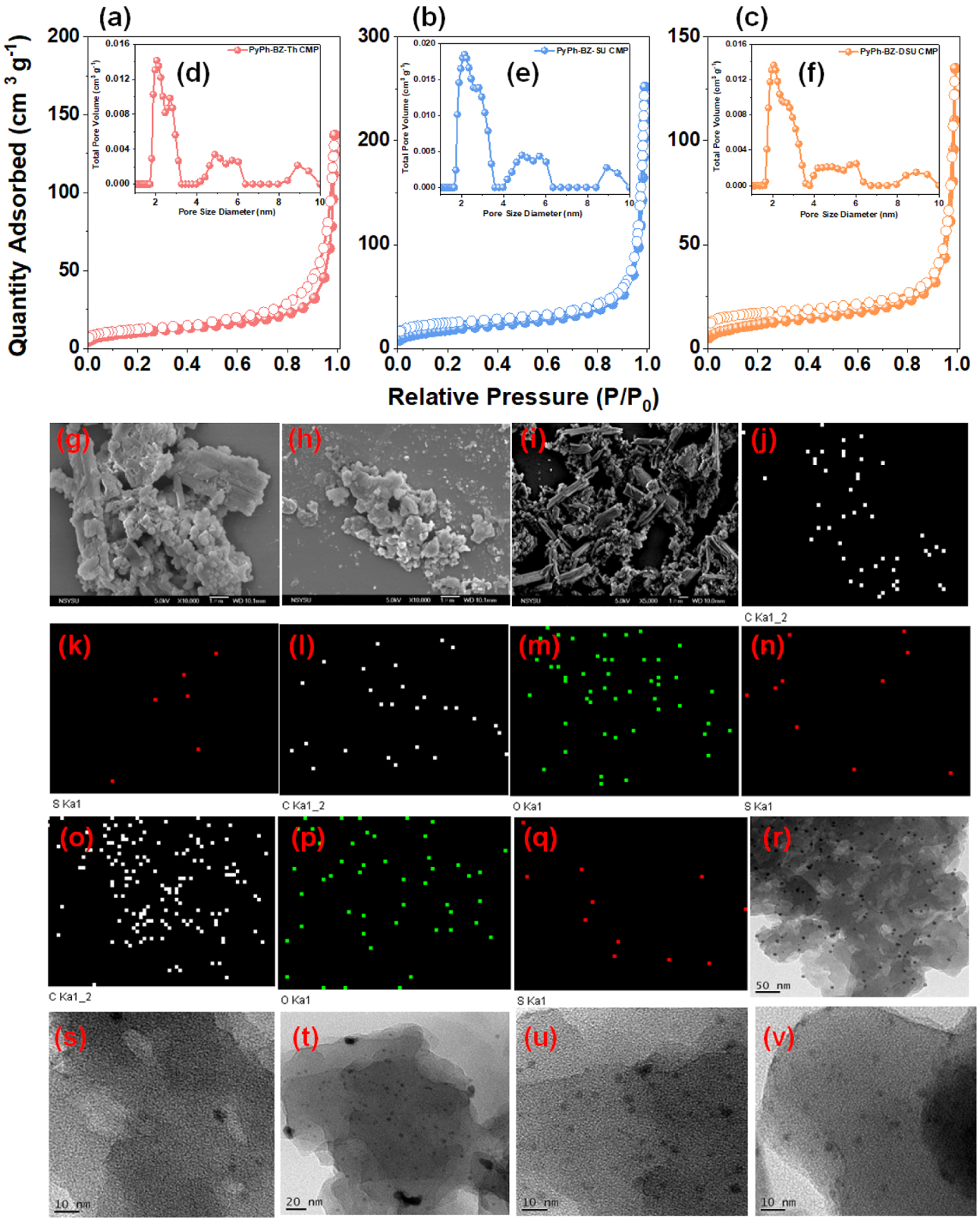

Figure 3. (a–c) N_2-adsorption–desorption isotherms, (d–f) pore size diameters, (g–i) SEM images, (j–q) SEM-EDS images, and (r–v) TEM images of (a,d,g,j,k,r,s) PyPh-BZ-Th CMP, (b,e,h,l,m,n,t,u) PyPh-BZ-SU CMP, and (c,f,o,p,q,v) PyPh-BZ-DSU CMP.

and 26.8% for PyPh-BZ-SU, and 59.37, 10.5, and 30.1% for PyPh-BZ-DSU, respectively. Meanwhile, the weight percentages for C and O in the PyPh-BZ-Th CMP were 69.51 and 30.4%, respectively.

Using N_2 isotherms, we investigated the intricate pore characteristics of the PyPh-BZ-Th, PyPh-BZ-SU, and PyPh-BZ-DSU CMPs. BET computation and the NLDFT model were employed to examine the SSA (S_{BET}), total pore volume (TPV), and average pore size (APS) [Figure 3a–f],

https://doi.org/10.1021/acsapm.4c02368
ACS Appl. Polym. Mater. 2024, 6, 12247–12260

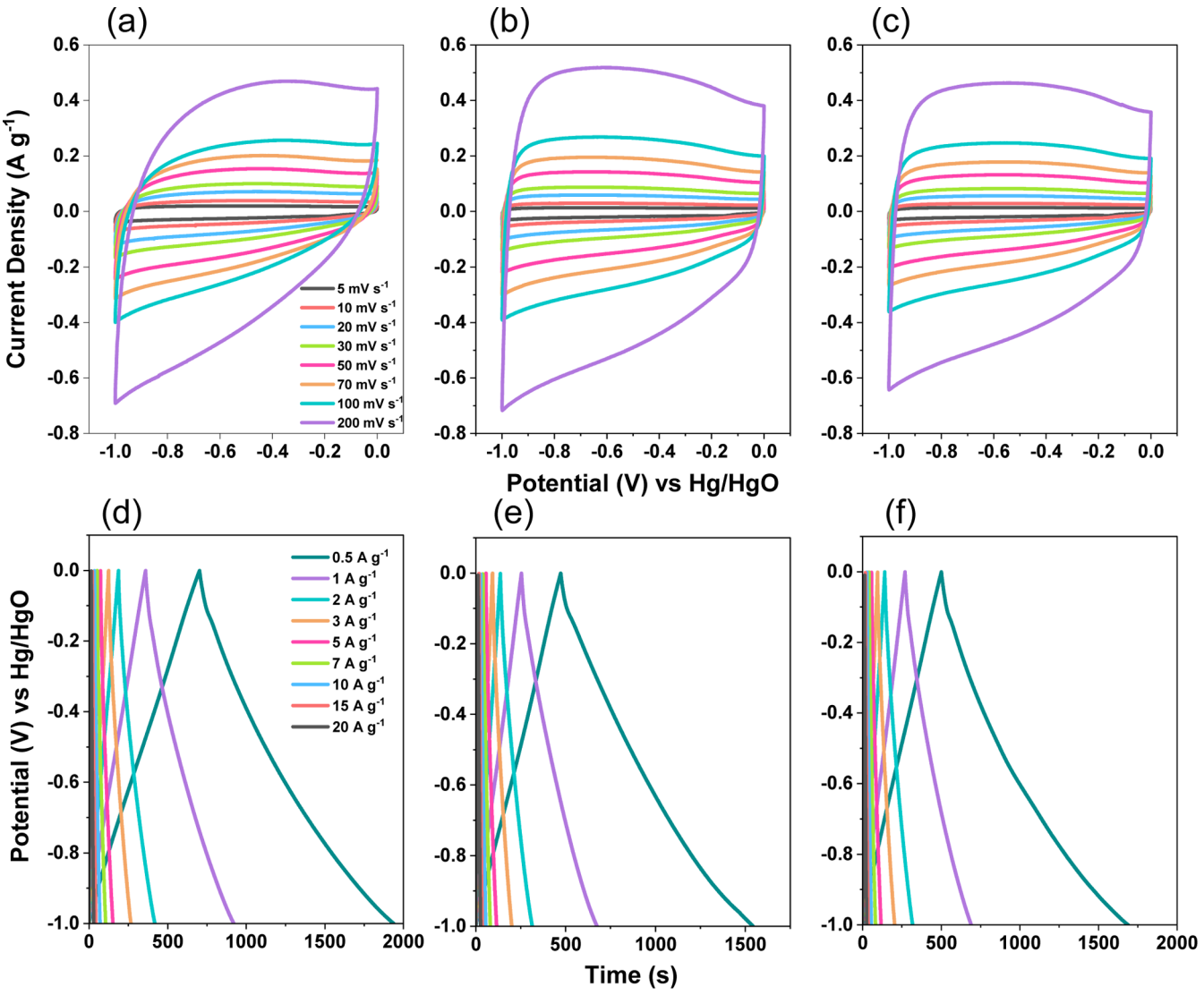

Figure 4. (a–c) CV and (d–f) GCD profiles of (a,d) PyPh-BZ-Th CMP, (b,e) PyPh-BZ-SU CMP, and (c,f) PyPh-BZ-DSU CMP.

respectively. Figure 3a–c shows the I-type isothermal curves of PyPh-BZ-Th, PyPh-BZ-SU, and PyPh-BZ-DSU CMPs, respectively. The S_{BET}, TPV, and APS values for PyPh-BZ-Th CMP are 37 m^2 g^{-1}, 0.2 cm^3 g^{-1}, and 2.04 nm [Figure 3d], respectively. For PyPh-BZ-SU CMP, the values are 65 m^2 g^{-1}, 0.3 cm^3 g^{-1}, and 2.1 nm [Figure 3e], and for PyPh-BZ-DSU CMP, the values are 42 m^2 g^{-1}, 0.19 cm^3 g^{-1}, and 2.03 nm [Figure 3f]. SEM, SEM-EDS mapping, and TEM were employed to examine the morphologies and elemental compositions (C, S, and O) of the CMPs. SEM images of PyPh-BZ-Th and PyPh-BZ-SU CMPs show the aggregation of irregular spherical structures [Figure 3g,h], whereas SEM images of PyPh-BZ-DSU CMP display a nanorod morphology, attributed to the $\pi-\pi$ stacking interactions among the polymer chains [Figure 3i]. SEM-EDS images confirm the presence of carbon (C, white color) and sulfur (S, red color) in the PyPh-BZ-Th CMP structure [Figure 3j,k] and C, O, and S in the conjugated network of PyPh-BZ-SU [Figure 3l–n] and PyPh-BZ-DSU CMPs [Figure 3o–q]. However, TEM images did not reveal a specifically ordered structure for any of the CMPs [Figure 3r–v]. XRD analysis of PyPh-BZ-Th, PyPh-BZ-SU, and PyPh-BZ-DSU CMPs revealed no specific diffraction peaks, displaying instead a broad halo that indicates the amorphous nature of the regions where the polymer chains are randomly organized without any long-range order [Figure S11].[30,58] The wettability of the PyPh-BZ-Th, PyPh-BZ-SU, and PyPh-BZ-DSU CMPs was evaluated by using water contact angle (WCA) measurements. The WCA values obtained for PyPh-BZ-Th, PyPh-BZ-SU, and PyPh-BZ-DSU were 81.1°, 78.2°, and 67.7°, respectively, as shown in Figure S12.

Electrochemical Performance of PyPh-BZ-Th CMP, PyPh-BZ-SU CMP, and PyPh-BZ-DSU CMP Based on Three-Electrode System and Symmetric Coin Cell. The electrochemical properties of PyPh-BZ-Th CMP, PyPh-BZ-SU CMP, and PyPh-BZ-DSU CMP are analyzed by using CV and GCD techniques. The CV profiles of the CMPs, illustrated in Figure 4a–c, are observed in a potential window from −1 to 0 V across various scan rates from 5 to 200 mV s^{-1}, exhibiting rectangular shapes without significant peaks, indicative of dominant EDLC behavior. In cyclic voltammetry, the voltage is alternated cyclically between predetermined upper and lower limits, termed oxidation, and reduction potentials, respectively.[52,67,68] The voltage linearly sweeps from the starting potential to the upper potential (oxidation phase) and then reverses to sweep down to the lower potential (reduction

https://doi.org/10.1021/acsapm.4c02368
ACS Appl. Polym. Mater. 2024, 6, 12247−12260

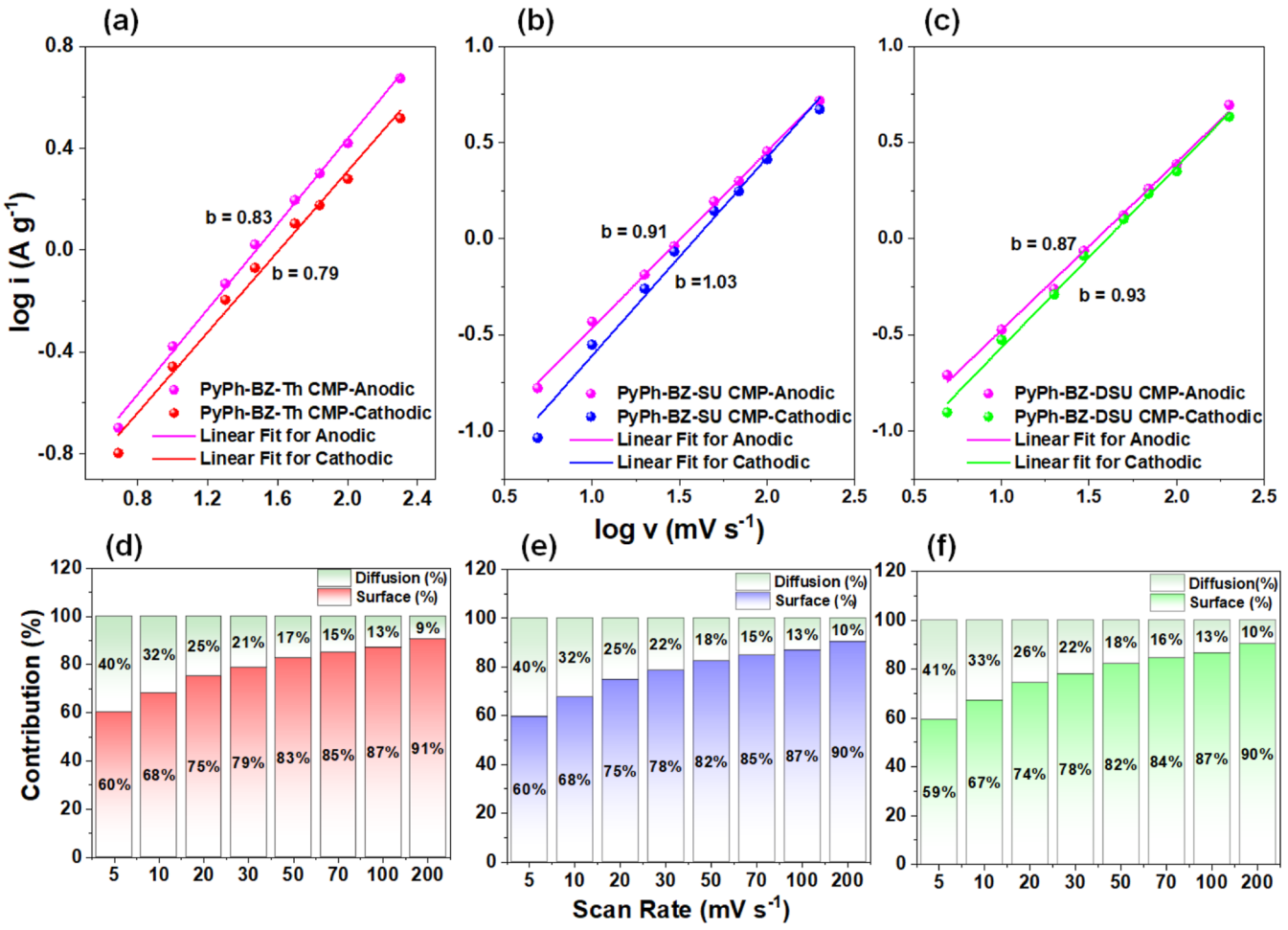

Figure 5. (a–c) Plots of log i vs log v and (d–f) analyses of the relative contributions of capacitive and diffusion-controlled charge storage (recorded at various scan rates) for (a,d) PyPh-BZ-Th CMP, (b,e) PyPh-BZ-SU CMP, and (c,f) PyPh-BZ-DSU CMP.

phase) for various scan rates. The capacitance of EDLC, which is a critical measure of its electrochemical performance, can be inferred from the area under the cyclic voltammogram. A larger area under the curve suggests a higher capacitance. However, the specific current decreases with a reduction in scan rate, as evidenced by the figures, which implies a decrease in capacitance. During the GCD test, a constant current is applied to the SC during the charging phase, causing the voltage to increase linearly with time. In the discharge phase, the current is reversed, resulting in a linear decrease in the voltage. The voltage–time curve obtained during charge and discharge provides specific insights into the SC's behavior. The GCD profiles of PyPh-BZ-Th, PyPh-BZ-SU, and PyPh-BZ-DSU CMPs showed perfectly triangular discharging curves [Figure 4d–f].

After conducting the electrochemical analysis, further investigation was performed to assess the capacitive contribution to overall charge storage using the power law expressed in eq 1

$$i = av^b \tag{1}$$

where a and b are constants and b represents the slope calculated by plotting log(i) vs log(v). This power law equation was employed to examine the charge storage capabilities of the electrodes (Figure 5). The calculated slopes for the cathodic line are 0.79, 1.03, and 0.93 for the PyPh-BZ-Th CMP, PyPh-BZ-SU CMP, and PyPh-BZ-DSU CMP, respectively. For the anodic line, the slopes are 0.83, 0.91, and 0.87 for PyPh-BZ-Th CMP, PyPh-BZ-SU CMP, and PyPh-BZ-DSU CMP, respectively [Figure 5a–c]. When the slope is less than or equal to 0.5, diffusion control is dominant, which is typically observed in pseudocapacitive materials. However, in this case, the charge storage mechanism predominantly operates under capacitive or surface control. The percentage distribution of surface and diffusive control is calculated using the following eq 2

$$i(V) = k_1 v + k_2 v^{1/2} \tag{2}$$

where k_1 is the slope and k_2 is the intercept of the fitted line of the log(i) vs log(v) plot. Figure 5d–f shows the percentage contribution of PyPh-BZ-Th, PyPh-BZ-SU, and PyPh-BZ-DSU CMPs. PyPh-BZ-Th CMP displays a 60% surface-controlled distribution at 5 mV s^{-1}, which increases to 91% at 200 mV s^{-1}. For PyPh-BZ-SU CMP and PyPh-BZ-DSU CMP, the surface-controlled distributions are 60 and 59% at 5 mV s^{-1}, increasing to 90% at 200 mV s^{-1}. The higher capacitive-controlled contribution is ascribed to the S and SO_2 groups' existence in the cross-linked network of CMPs, which enhances electrostatic interaction.

As illustrated in Figure 4d–f, the GCD plots of PyPh-BZ-Th, PyPh-BZ-SU, and PyPh-BZ-DSU CMPs (from 0.5 to 20 A g^{-1}) are displayed. Using the discharge times of the GCD

https://doi.org/10.1021/acsapm.4c02368
ACS Appl. Polym. Mater. 2024, 6, 12247–12260

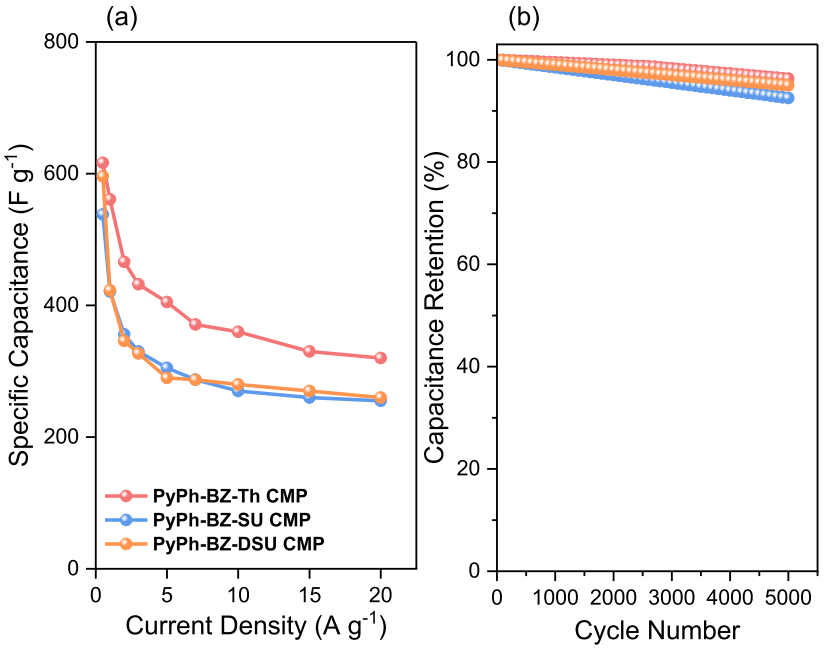

Figure 6. (a) Specific capacitance and (b) capacitance retention (recorded after 5000 cycles) plots of PyPh-BZ-Th CMP, PyPh-BZ-SU CMP, and PyPh-BZ-DSU CMP.

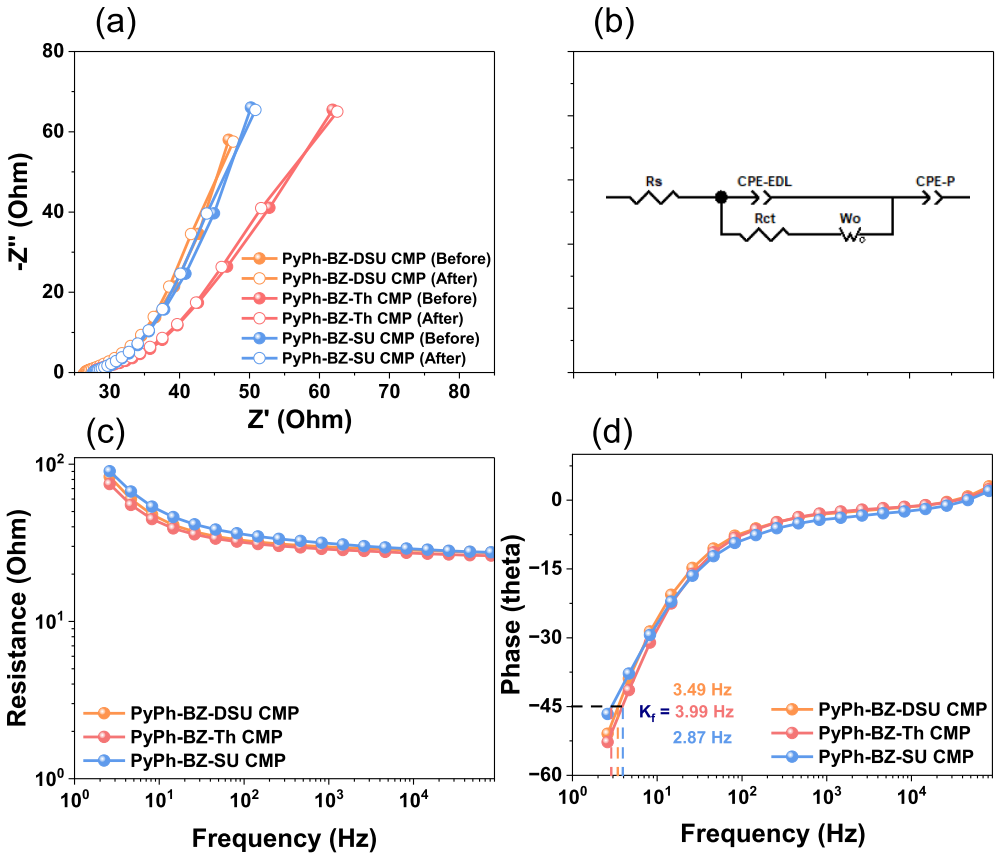

Figure 7. EIS plots: (a) Nyquist plots and (b) equivalent fitted circuit, (c) Bode plot of frequency-dependent resistance (magnitude), and (d) Bode plot of frequency-dependent phase angles of PyPh-BZ-DSU CMP, PyPh-BZ-Th CMP, and PyPh-BZ-SU CMP.

profiles, we calculated specific capacitances of 617, 538, and 596 F g^{-1} for PyPh-BZ-Th CMP, PyPh-BZ-SU CMP, and PyPh-BZ-DSU CMP, respectively, at 0.5 A g^{-1}. Upon increasing the current density to 20 A g^{-1}, a reduction in capacitance was noted, resulting in values of 320, 255, and 260 F g^{-1} for PyPh-BZ-Th CMP, PyPh-BZ-SU CMP, and PyPh-BZ-DSU CMP, respectively [Figure 6a]. This decline in capacitance at higher current densities is attributed to the reduced time available for electrolyte ions to diffuse and reach the electrode surfaces. Consequently, the electrode surface area

https://doi.org/10.1021/acsapm.4c02368
ACS Appl. Polym. Mater. 2024, 6, 12247−12260

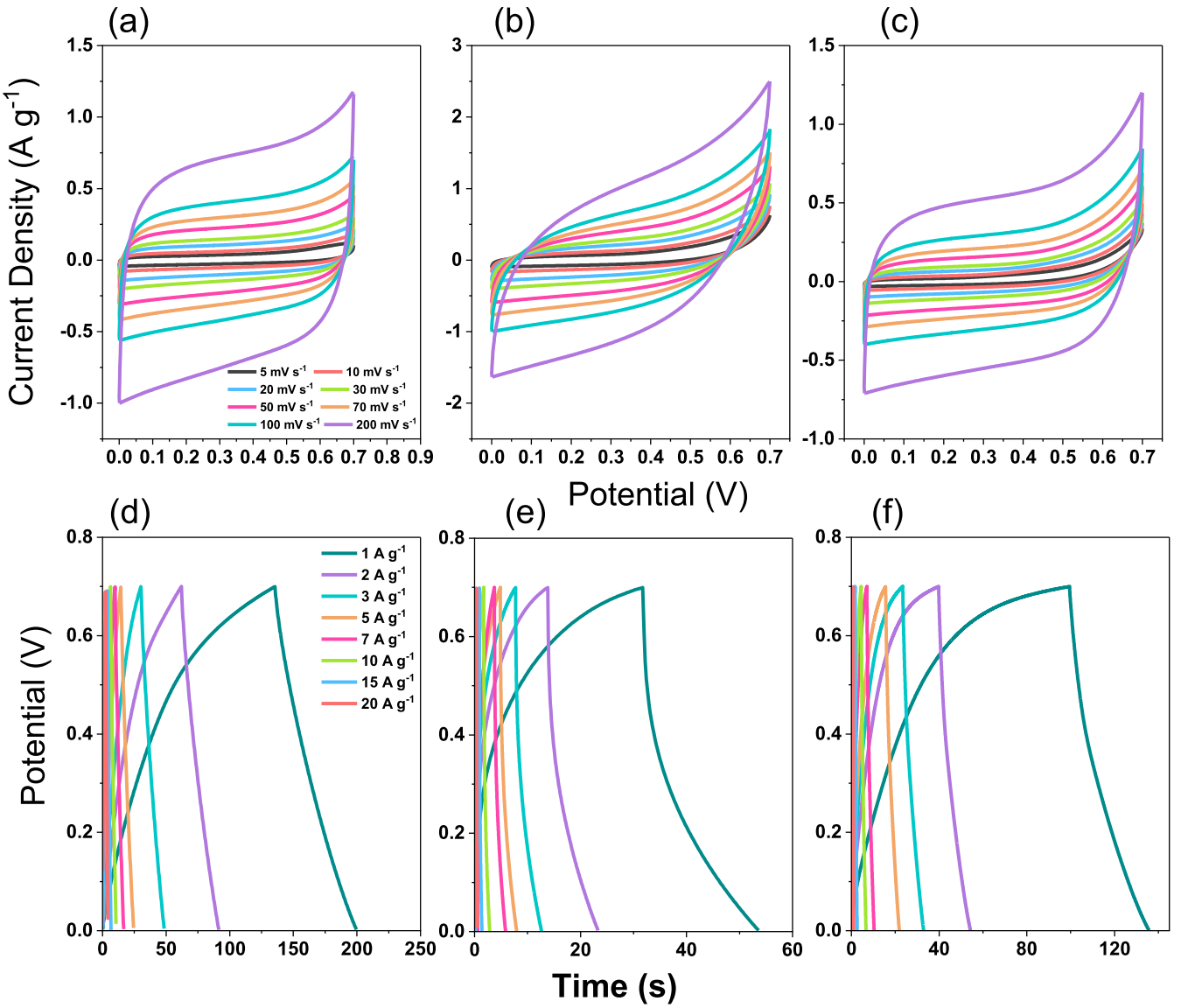

Figure 8. (a–c) CV and (d–f) GCD profiles of (a,d) PyPh-BZ-Th CMP, (b,e) PyPh-BZ-SU CMP, and (c,f) PyPh-BZ-DSU CMP based on a symmetric supercapacitor coin cell.

is not fully utilized for charge storage, leading to a decrease in effective capacitance. Additionally, the resistance of both the electrode material and the electrolyte becomes more significant at higher current rates, causing voltage drops across the electrode–electrolyte interfaces. This increased resistance impacts the overall charge storage capacity, resulting in a decrease in the specific capacitance. The high electronegativity of S atoms and the polar nature of SO_2 groups enhance electrostatic interactions with electrolyte ions, leading to improved ion adsorption and retention at the electrode surface, thereby increasing capacitance. Sulfone (SO_2) groups also enhance the wettability of the electrode material, ensuring better contact with the electrolyte and facilitating more effective ion transport.[57,58,69,70] Furthermore, adding sulfur to CMP materials can enhance their overall electrical conductivity and create clearly defined channels for ion transfer.[69,70] Improved conductivity reduces internal resistance, thereby enhancing the efficiency of charge storage and retrieval. Table S1 illustrates that the high capacitance values of PyPh-BZ-Th, PyPh-BZ-SU, and PyPh-BZ-DSU CMPs at 0.5 A g^{-1} are comparable to those found in other CMP materials. The percentage of capacitance retention (%) is also evaluated over 5000 cycles to assess the long-term stability of the electrodes. A high capacitance retention percentage signifies excellent stability and minimal degradation of capacitance over time or cycles, which is essential for ensuring reliability and durability, particularly in applications that demand frequent cycling or extended usage. The capacitance retention percentages are 96.3, 93, and 95% for PyPh-BZ-Th CMP, PyPh-BZ-SU CMP, and PyPh-BZ-DSU CMP, respectively (Figure 6b). Based on these results, it can be concluded that PyPh-BZ-Th CMP is a leading material for SC applications.

Electrochemical impedance spectroscopy (EIS) was employed to investigate the electrochemical properties of PyPh-BZ-DSU, PyPh-BZ-Th, and PyPh-BZ-SU CMPs using a three-electrode setup. This technique provided insights into the materials' impedance, capacitance, and resistance across a range of frequencies. Nyquist plots for the CMPs (PyPh-BZ-DSU, PyPh-BZ-Th, and PyPh-BZ-SU CMPs) are depicted in Figure 7a, both before and after fitting to the equivalent circuit

https://doi.org/10.1021/acsapm.4c02368
ACS Appl. Polym. Mater. 2024, 6, 12247–12260

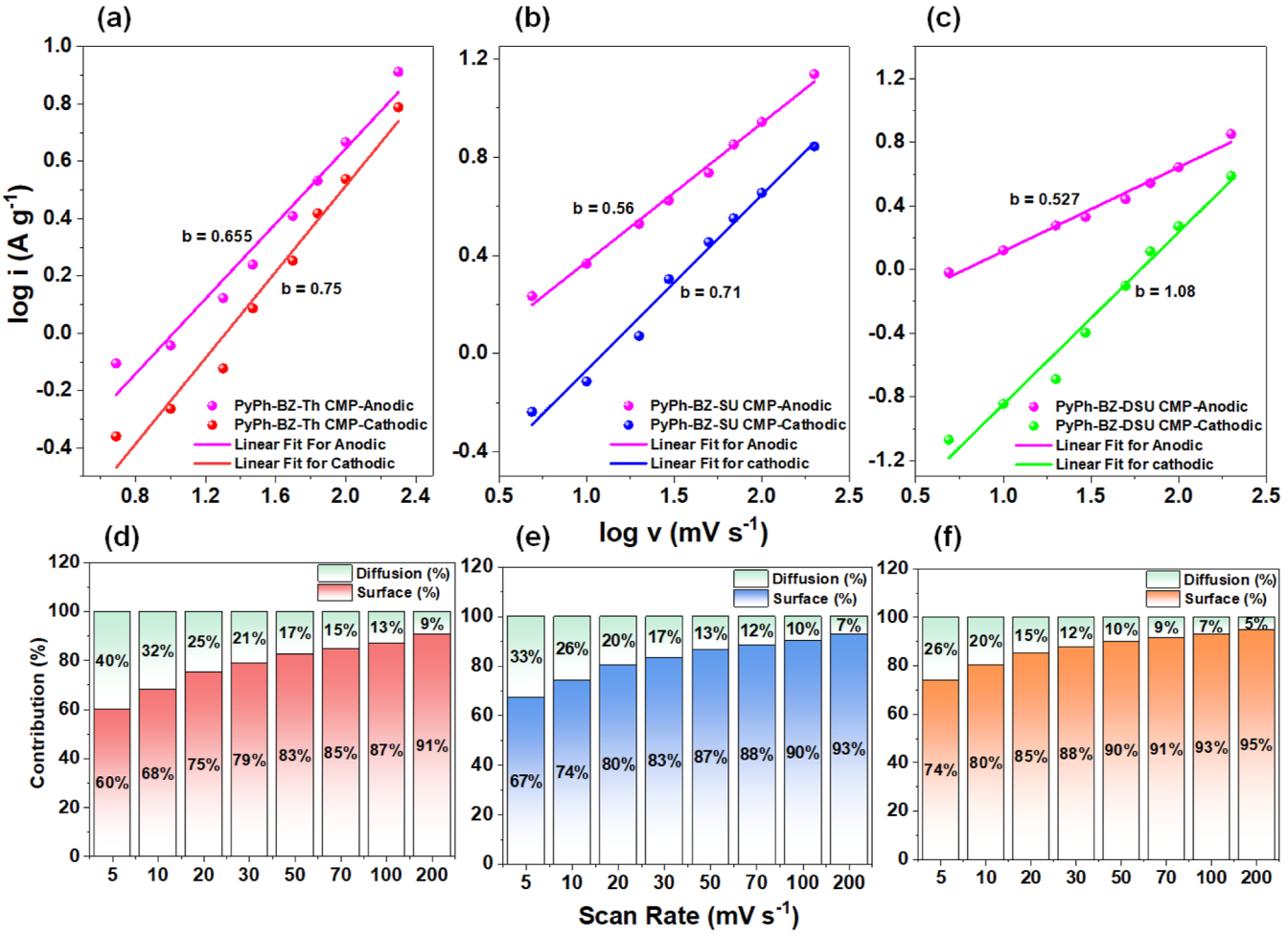

Figure 9. (a–c) Plots of log *i* vs log *v* and (d–f) analyses of the relative contributions of capacitive and diffusion-controlled charge storage (recorded at various scan rates) for (a,d) PyPh-BZ-Th CMP, (b,e) PyPh-BZ-SU CMP, and (c,f) PyPh-BZ-DSU CMP based on a symmetric supercapacitor coin cell.

model, as shown in Figure 7b. In the three-electrode system, the equivalent circuit used for fitting included several components: series resistance (Rs), charge transfer resistance (Rct), constant phase elements (CPE-EDL and CPE-P), and the Warburg element (Zw). The Rs, representing the Ohmic resistance of the electrolyte and cell components, were found to be 26.97, 26.26, and 27.51 Ohms for PyPh-BZ-DSU, PyPh-BZ-Th, and PyPh-BZ-SU CMPs, respectively [Table S2]. The conductivities of the PyPh-BZ-DSU, PyPh-BZ-Th, and PyPh-BZ-SU CMPs were measured at 0.037, 0.039, and 0.036 S/cm, respectively. This indicates that the overall resistance due to the electrolyte and cell components is relatively low and consistent. Charge transfer resistance (Rct) is crucial for understanding the ease of electron movement across the electrode–electrolyte interface. The Rct values differed significantly, with PyPh-BZ-SU CMP showing 434 Ohms, while PyPh-BZ-DSU and PyPh-BZ-Th CMPs exhibited much lower Rct values of 293.4 and 268.2 Ohms, respectively, suggesting better electron transfer and conductivity in the latter. The constant phase elements, CPE-EDL and CPE-P, account for the nonideal capacitive behavior at the electrode–electrolyte interface and within the porous structure of the electrode, respectively. The Warburg element (Zw) indicates that diffusion processes occur within the electrode materials. Furthermore, the Bode plots shown in Figure 7c illustrate significant resistance at higher frequencies and descending slopes at lower frequencies, indicating the impedance behavior across various frequencies, indicative of excellent capacitive properties for all CMP materials tested. The phase-angle Bode graphs (Figure 7d) display the knee frequencies, which indicate the rate performance of the electrode materials. Higher knee frequencies correspond to better rate performance. The results show that all the electrodes deliver almost the same knee frequencies, suggesting ideal behavior.

To further enhance the investigation, we focused on constructing a SC coin cell. These characteristics are essential for maximizing the charge storage capacity and overall efficiency. The CV profiles, shown in Figure 8a–c, display a wider potential window of 0 to 0.7 V for PyPh-BZ-Th, PyPh-BZ-SU, and PyPh-BZ-DSU CMPs, respectively. The rectangular shape of the CV profiles indicates a prominent EDLC behavior. EDLC stores energy through physical charge separation occurring at the interface between the electrode and electrolyte, unlike the chemical reactions typical in batteries. This separation creates an EDL consisting of ions from the electrolyte attracted to oppositely charged sites on the electrode surface. An increase in the specific current with an increasing scan rate is observed in the CV profiles of all CMPs. The GCD of PyPh-BZ-Th, PyPh-BZ-SU, and PyPh-BZ-DSU CMPs revealed perfectly triangular discharging curves [Figure

https://doi.org/10.1021/acsapm.4c02368
ACS Appl. Polym. Mater. 2024, 6, 12247–12260

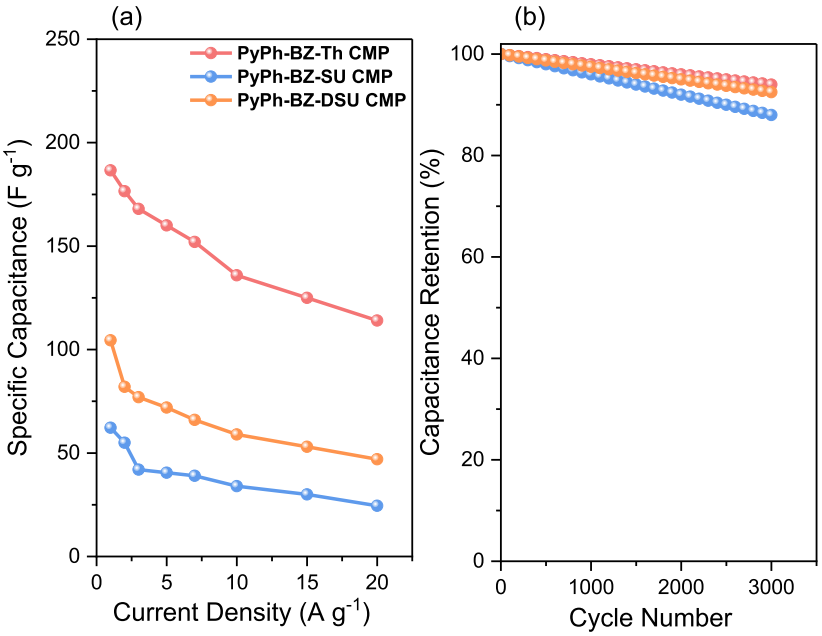

Figure 10. (a) Specific capacitance and (b) capacitance retention (recorded after 3000 cycles) plots of PyPh-BZ-Th, PyPh-BZ-SU, and PyPh-BZ-DSU CMPs based on a symmetric supercapacitor coin cell.

8d–f], indicating reversible ionic adsorption and desorption mechanisms and effective ion transport.

The power law equation (eq 1) was utilized to evaluate the charge storage performance of PyPh-BZ-Th CMP, PyPh-BZ-SU CMP, and PyPh-BZ-DSU CMP as organic electrodes in symmetric coin cells [Figure 9a–c]. The slopes calculated for the cathodic line were 0.75 for PyPh-BZ-Th CMP, 0.71 for PyPh-BZ-SU CMP, and 1.03 for PyPh-BZ-DSU CMP. Correspondingly, the slopes for the anodic line were 0.66, 0.56, and 0.53. Typically, a slope less than or equal to 0.5 indicates dominant diffusion control, commonly seen in pseudocapacitive materials. However, charge storage predominantly functioned under capacitive or surface control mechanisms in this study. Figure 9d–f illustrates the percentage contributions for all CMPs. PyPh-BZ-Th CMP showed a 60% surface-controlled distribution at 5 mV s^{-1}, escalating to 91% at 200 mV s^{-1}. Similarly, PyPh-BZ-SU CMP and PyPh-BZ-DSU CMP displayed surface-controlled distributions of 67 and 74% at 5 mV s^{-1}, respectively, which increased to 93 and 95% at 200 mV s^{-1}.

As presented in Figure 10a, symmetric devices were constructed for all CMPs to evaluate their practical performance, with specific capacitances derived from GCD curves recorded at 187 F g^{-1} for the PyPh-BZ-Th CMP, 63 F g^{-1} for the PyPh-BZ-SU CMP, and 105 F g^{-1} for the PyPh-BZ-DSU CMP. High cycle stability is crucial for ensuring the long-term reliability and durability of SCs, especially in applications that require frequent cycling or extended usage. Stability is evaluated over 3000 GCD cycles to measure the capacitance retention (%) for all CMPs. The capacitance retention rates are 94, 88, and 92.2% for PyPh-BZ-Th, PyPh-BZ-SU, and PyPh-BZ-DSU CMPs, respectively (Figure 10b).

Figure S13 presents the Ragone plot for all of the CMPs. Among them, PyPh-BZ-Th CMP demonstrates outstanding performance, achieving an energy density of 12.73 W h kg^{-1} at a power density of 709 W kg^{-1}. As the power density increases to 14626 W kg^{-1}, the energy density decreases to 7.76 W h kg^{-1}. This remarkable performance is due to the structure of the PyPh-BZ-Th CMP, which contains highly electronegative moieties that enhance electrostatic interactions on the electrode surface. This characteristic makes it ideal for applications that prioritize power delivery over total energy storage capacity, where frequent cycling and rapid response times are crucial. In contrast, the PyPh-BZ-SU CMP and PyPh-BZ-DSU CMP exhibit energy densities of 4.29 and 7.15 W h kg^{-1}, respectively, at a power density of 709 W kg^{-1}. When the power density increases to 14,626 W kg^{-1}, their energy densities decrease to 1.7 and 4.29 W h kg^{-1}, respectively, as illustrated in Figure S13. For the symmetric coin cell configuration, EIS was conducted to investigate the electrochemical behavior under practical device conditions. Nyquist plots for PyPh-BZ-DSU, PyPh-BZ-Th, and PyPh-BZ-SU CMPs in symmetric coin cells are shown in Figure S14a, both before and after fitting to the equivalent circuit model, as shown in Figure S14b. In the coin cell setup, the same equivalent circuit model was used to fit the EIS data. The series resistance and Rs values [Table S3] were found to be 1.17, 0.76, and 3.11 Ohms for PyPh-BZ-DSU, PyPh-BZ-Th, and PyPh-BZ-SU CMPs, respectively, indicating similar Ohmic resistances across all cases. The conductivities of the PyPh-BZ-DSU, PyPh-BZ-Th, and PyPh-BZ-SU CMPs were measured at 0.85, 1.32, and 0.32 S/cm, respectively. However, significant differences were observed in the Rct, with PyPh-BZ-Th CMP exhibiting a substantially lower Rct of 10.07 Ohms compared to PyPh-BZ-DSU CMP at 14.55 Ohms and PyPh-BZ-SU CMP at 43.37 Ohms. This substantial difference underscores the superior conductivity and lower charge transfer resistance of PyPh-BZ-Th CMP. The Bode plots [Figure S14c] show the impedance magnitude across a range of frequencies, revealing negative slopes at low frequencies and notable resistance at higher frequencies, indicative of exceptional capacitive properties in all CMP materials evaluated. The phase-angle Bode graphs [Figure S14d] illustrate the knee frequencies, which are critical for assessing the rate performance of the electrode materials. Higher knee frequencies are associated with enhanced rate capabilities. For the PyPh-BZ-DSU, PyPh-BZ-

https://doi.org/10.1021/acsapm.4c02368
ACS Appl. Polym. Mater. 2024, 6, 12247–12260

Th, and PyPh-BZ-SU CMPs, the knee frequencies were determined to be 3.41, 35.8, and 3.7 Hz, respectively, highlighting the superior rate performance of the PyPh-BZ-Th CMP.

CONCLUSIONS

We successfully synthesized PyPh-BZ-Th, PyPh-BZ-SU, and PyPh-BZ-DSU CMPs through the Suzuki coupling technique. Their molecular architectures were confirmed with FTIR and CPMAS ^{13}C NMR analyses. Electrochemical properties were evaluated using CV and GCD methods. From the GCD tests at 0.5 A g^{-1}, the specific capacitances recorded were 617, 538, and 596 F g^{-1} for PyPh-BZ-Th, PyPh-BZ-SU, and PyPh-BZ-DSU CMPs. We also constructed symmetric devices for each type of CMP to examine their practical performance. These devices showed specific capacitances of 187, 63, and 105 F g^{-1} for PyPh-BZ-Th, PyPh-BZ-SU, and PyPh-BZ-DSU CMPs in GCD tests. Notably, PyPh-BZ-Th CMP demonstrated a high power density of 14626 W kg^{-1} and an energy density of 12.73 W h kg^{-1}, maintaining 94% capacitance after 3000 GCD cycles. This investigation underscores the enhanced potential of Th and DSU-based CMPs in pushing forward the boundaries of energy storage technology.

ASSOCIATED CONTENT

Supporting Information

The Supporting Information is available free of charge at https://pubs.acs.org/doi/10.1021/acsapm.4c02368.

Experimental details include characterizations, electrochemical analysis, measurements, and synthetic schemes of PyPh-Br_4, Th-Br_2, SU-Br_2, DSU-Br_2, PyPh-BZ-Th CMP, PyPh-BZ-SU CMP, and PyPh-BZ-DSU CMP, along with FTIR and NMR data for PyPh-Br_4, Th-Br_2, SU-Br_2, and DSU-Br_2; XRD, WCA, and Ragone plot for PyPh-BZ-Th, PyPh-BZ-SU, and PyPh-BZ-DSU CMPs, as well as a performance comparison of SCs using PyPh-BZ-Th, PyPh-BZ-SU, and PyPh-BZ-DSU CMP electrodes with previously described electrodes (PDF)

AUTHOR INFORMATION

Corresponding Author

Shiao-Wei Kuo − *Department of Materials and Optoelectronic Science, Center for Functional Polymers and Supramolecular Materials, National Sun Yat-Sen University, Kaohsiung 804, Taiwan; Department of Medicinal and Applied Chemistry, Kaohsiung Medical University, Kaohsiung 807, Taiwan;* orcid.org/0000-0002-4306-7171; Email: kuosw@faculty.nsysu.edu.tw

Authors

Abdul Basit − *Department of Materials and Optoelectronic Science, Center for Functional Polymers and Supramolecular Materials, National Sun Yat-Sen University, Kaohsiung 804, Taiwan*

Mohamed Gamal Mohamed − *Department of Materials and Optoelectronic Science, Center for Functional Polymers and Supramolecular Materials, National Sun Yat-Sen University, Kaohsiung 804, Taiwan; Department of Chemistry, Faculty of Science, Assiut University, Assiut 71516, Egypt;* orcid.org/0000-0003-0301-8372

Santosh U. Sharma − *Institute of Chemistry, Academia Sinica, Taipei 115, Taiwan*

Complete contact information is available at: https://pubs.acs.org/10.1021/acsapm.4c02368

Author Contributions

⊥A.B. and M.G.M. contributed equally to this work.

Notes

The authors declare no competing financial interest.

ACKNOWLEDGMENTS

This study was supported financially by the National Science and Technology Council, Taiwan, under contracts NSTC 112-2223-E-110-002- and 112-2218-E-110-007. The authors thank the staff at National Sun Yat-sen University for their assistance with the TEM (ID: EM022600) experiments.

REFERENCES

(1) Yu, Z.; Tetard, L.; Zhai, L.; Thomas, J. Supercapacitor electrode materials: Nanostructures from 0 to 3 dimensions. *Energy Environ. Sci.* **2015**, *8*, 702−730.

(2) Samy, M. M.; Mohamed, M. G.; Sharma, S. U.; Chaganti, S. V.; Lee, J. T.; Kuo, S. W. An Ultrastable Tetrabenzonaphthalene-Linked conjugated microporous polymer functioning as a high-performance electrode for supercapacitors. *J. Taiwan Inst. Chem. Eng.* **2024**, *158*, 104750.

(3) Samy, M. M.; Mohamed, M. G.; Kuo, S. W. Pyrene-functionalized tetraphenylethylene polybenzoxazine for dispersing single-walled carbon nanotubes and energy storage. *Compos. Sci. Technol.* **2020**, *199*, 108360.

(4) Mousa, A. O.; Sharma, S. U.; Chaganti, S. V.; Mansoure, T. H.; Singh, P. N.; Ejaz, M.; Chuang, C. H.; Lee, J. T.; Kuo, S. W.; Mohamed, M. G. Designing strategically functionalized conjugated microporous polymers with pyrene and perylenetetracarboxylic dianhydride moieties with single-walled carbon nanotubes to enhance supercapacitive energy storage efficiency. *J. Power Sources* **2024**, *608*, 234624.

(5) Zhao, M.; Zhao, Q.; Li, B.; Xue, H.; Pang, H.; Chen, C. Recent progress in layered double hydroxide-based materials for electrochemical capacitors: Design, synthesis and performance. *Nanoscale* **2017**, *9*, 15206−15225.

(6) Singh, P. N.; Mohamed, M. G.; Kuo, S. W. Systematic Design and Synthesis of Conjugated Microporous Polymers Containing Pyrene and Azobenzene Building Materials for High-Performance Energy Storage. *ACS Appl. Energy Mater.* **2023**, *6*, 11342−11351.

(7) Libich, J.; Máca, J.; Vondrák, J.; Čech, O.; Sedlaříková, M. Supercapacitors: Properties and applications. *J. Energy Storage* **2018**, *17*, 224−227.

(8) Ejaz, M.; Mohamed, M. G.; Chen, Y. T.; Zhang, K.; Kuo, S. W. Porous carbon materials augmented with heteroatoms derived from hyperbranched biobased benzoxazine resins for enhanced CO_2 adsorption and exceptional supercapacitor performance. *J. Energy Storage* **2024**, *78*, 110166.

(9) Mohamed, M. G.; Mansoure, T. H.; Takashi, Y.; Mohamed Samy, M.; Chen, T.; Kuo, S. W. Ultrastable porous organic/inorganic polymers based on polyhedral oligomeric silsesquioxane (POSS) hybrids exhibiting high performance for thermal property and energy storage. *Microporous Mesoporous Mater.* **2021**, *328*, 111505.

(10) Wang, S. H.; Li, L.; Wang, H.; Wang, X. W.; Wang, T. H. Continuous and Scalable Manufacture of Coal-Derived Hierarchical Porous Carbon Dominated with Mesopores for High Rate-Performance Supercapacitors. *ACS Appl. Energy Mater.* **2024**, *7*, 4268−4278.

(11) Wang, F.; Wu, X.; Yuan, X.; Liu, Z.; Zhang, Y.; Fu, L.; Zhu, Y.; Zhou, Q.; Wu, Y.; Huang, W. Latest advances in supercapacitors: from new electrode materials to novel device designs. *Chem. Soc. Rev.* **2017**, *46*, 6816−6854.

(12) Liu, C.; Bai, Y.; Li, W.; Yang, F.; Zhang, G.; Pang, H. In situ growth of three-dimensional MXene/metal−organic framework

composites for high-performance supercapacitors. *Angew. Chem., Int. Ed.* **2022**, *61*, No. e202116282.
(13) Samy, M. M.; Mohamed, M. G.; Kuo, S. W. Directly synthesized nitrogen-and-oxygen−doped microporous carbons derived from a bio-derived polybenzoxazine exhibiting high-performance supercapacitance and CO_2 uptake. *Eur. Polym. J.* **2020**, *138*, 109954.
(14) Mohamed, M. G.; Mansoure, T. H.; Samy, M. M.; Takashi, Y.; Mohammed, A. A. K.; Ahamad, T.; Alshehri, S. M.; Kim, J.; Matsagar, B. M.; Wu, K. C. W.; Kuo, S. W. Ultrastable Conjugated Microporous Polymers Containing Benzobisthiadiazole and Pyrene Building Blocks for Energy Storage Applications. *Molecules* **2022**, *27*, 2025.
(15) Mohamed, M. G.; Sharma, S. U.; Liu, N. Y.; Mansoure, T. H.; Samy, M. M.; Chaganti, S. V.; Chang, Y. L.; Lee, J. T.; Kuo, S. W. Ultrastable Covalent Triazine Organic Framework Based on Anthracene Moiety as Platform for High-Performance Carbon Dioxide Adsorption and Supercapacitors. *Int. J. Mol. Sci.* **2022**, *23*, 3174.
(16) Mohamed, M. G.; Hu, H. Y.; Madhu, M.; Samy, M. M.; Mekhemer, I. M. A.; Tseng, W. L.; Chou, H. H.; Kuo, S. W. Ultrastable Two-Dimensional Fluorescent Conjugated Microporous Polymers Containing Pyrene and Fluorene Units for Metal Ion Sensing and Energy Storage. *Eur. Polym. J.* **2023**, *189*, 111980.
(17) Mousa, A. O.; Mohamed, M. G.; Chuang, C. H.; Kuo, S. W. Carbonized Aminal-Linked Porous Organic Polymers Containing Pyrene and Triazine Units for Gas Uptake and Energy Storage. *Polymers* **2023**, *15*, 1891.
(18) Lin, M. C.; Kuo, S. W.; Mohamed, M. G. High-Performance Anthracene-Linked Covalent Triazine Framework with Dual Functions for CO_2 Capture and Supercapacitor Applications. *Mater. Adv.* **2024**, *5*, 6222−6233.
(19) Liu, S.; Kang, L.; Zhang, J.; Jung, E.; Lee, S.; Jun, S. C. Structural engineering and surface modification of MOF-derived cobalt-based hybrid nanosheets for flexible solid-state supercapacitors. *Energy Storage Mater.* **2020**, *32*, 167−177.
(20) Samy, M. M.; Mekhemer, I. M. A.; Mohamed, M. G.; Elsayed, M. H.; Lin, K. H.; Chen, Y. K.; Wu, T. L.; Chou, H. H.; Kuo, S. W. Conjugated microporous polymers incorporating Thiazolo [5,4-d] thiazole moieties for Sunlight-Driven hydrogen production from water. *Chem. Eng. J.* **2022**, *446*, 137158.
(21) Amin, K.; Ashraf, N.; Mao, L.; Faul, C. F. J.; Wei, Z. Conjugated microporous polymers for energy storage: Recent progress and challenges. *Nano Energy* **2021**, *85*, 105958.
(22) Samy, M. M.; Mohamed, M. G.; El-Mahdy, A. F. M.; Mansoure, T. H.; Wu, K. C. W.; Kuo, S. W. High-performance supercapacitor electrodes prepared from dispersions of tetrabenzonaphthalene-based conjugated microporous polymers and carbon nanotubes. *ACS Appl. Mater. Interfaces* **2021**, *13*, 51906−51916.
(23) Basit, A.; Mohamed, M. G.; Ejaz, M.; Xuan Su, B.; Manzoor, H.; Kuo, S. W. Boosting Supercapacitor Energy Storage Using Microporous Carbon Derived from an Octavinylsilsesquioxane and Fluorenone-Linked Porous Hybrid Polymer. *ACS Appl. Energy Mater.* **2024**, *7*, 7505−7516.
(24) Lin, Z.; Goikolea, E.; Balducci, A.; Naoi, K.; Taberna, P. L.; Salanne, M.; Yushin, G.; Simon, P. Materials for supercapacitors: When Li-ion battery power is not enough. *Mater. Today* **2018**, *21*, 419−436.
(25) Mohamed, M. G.; Samy, M. M.; Mansoure, T. H.; Li, C. J.; Li, W. C.; Chen, J. H.; Zhang, K.; Kuo, S. W. Microporous Carbon, and Carbon/Metal Composite Materials Derived from Bio-Benzoxazine-Linked Precursor for CO_2 Capture and Energy Storage Applications. *Int. J. Mol. Sci.* **2022**, *23*, 347.
(26) Mohamed, M. G.; Ahmed, M. M.; Du, W. T.; Kuo, S. W. Meso/Microporous Carbons from Conjugated Hyper-Crosslinked Polymers Based on Tetraphenylethene for High-Performance CO_2 Capture and Supercapacitor. *Molecules* **2021**, *26*, 738.
(27) Mohamed, M. G.; Samy, M. M.; Mansoure, T. H.; Sharma, S. U.; Tsai, M. S.; Chen, J. H.; Lee, J. T.; Kuo, S. W. Dispersions of 1,3,4-oxadiazole-linked conjugated microporous polymers with carbon nanotubes as a high-performance electrode for supercapacitors. *ACS Appl. Energy Mater.* **2022**, *5*, 3677−3688.
(28) Assresahegn, B. D.; Bélanger, D. Multifunctional Carbon for Electrochemical Double-Layer Capacitors. *Adv. Funct. Mater.* **2015**, *25*, 6775−6785.
(29) Lin, M. C.; Kuo, S. W.; Mohamed, M. G. High-performance anthracene-linked covalent triazine frameworks with dual functions for CO_2 capture and supercapacitor applications. *Mater. Adv.* **2024**, *5*, 6222−6233.
(30) Mohamed, M. G.; Chaganti, S. V.; Li, M. S.; Samy, M. M.; Sharma, S. U.; Lee, J. T.; Elsayed, M. H.; Chou, H. H.; Kuo, S. W. Ultrastable Porous Organic Polymers Containing Thianthrene and Pyrene Units as Organic Electrode Materials for Supercapacitors. *ACS Appl. Energy Mater.* **2022**, *5*, 6442−6452.
(31) Samy, M. M.; Gamal Mohamed, M.; Sharma, S. U.; Chaganti, S. V.; Hassan Mansoure, T.; Lee, J. T.; Chen, T.; Kuo, S. W. Constructing conjugated microporous polymers containing triphenylamine moieties for high-performance capacitive energy storage. *Polymer* **2023**, *264*, 125541.
(32) Mousa, A. O.; Chuang, C. H.; Kuo, S. W.; Mohamed, M. G. Strategic Design and Synthesis of Ferrocene Linked Porous Organic Frameworks toward Tunable CO_2 Capture and Energy Storage. *Int. J. Mol. Sci.* **2023**, *24*, 12371.
(33) Mohamed, M. G.; Sharma, S. U.; Wang, P. T.; Ibrahim, M.; Lin, M. H.; Liu, C. L.; Ejaz, M.; Yen, H. J.; Kuo, S. W. Construction of fully π-conjugated, diyne-linked conjugated microporous polymers based on tetraphenylethene and dibenzo[g,p]chrysene units for energy storage. *Polym. Chem.* **2024**, *15*, 2827−2839.
(34) Luo, B.; Chen, Y.; Zhang, Y.; Huo, J. Nitrogen-rich anthraquinone−triazine conjugated microporous polymer networks as high-performance supercapacitor. *New J. Chem.* **2021**, *45*, 17278−17286.
(35) Mohamed, M. G.; Ibrahim, M.; Ping Chen, N.; Basit, A.; Chin Kao, Y.; Osama Mousa, A.; Samy, M. M.; Kuo, S. W. Tetrabenzonaphthalene and Redox-Active Anthraquinone-Linked Conjugated Microporous Polymers as Organic Electrodes for Enhanced Energy Storage Efficiency. *ACS Appl. Energy Mater.* **2024**, *7*, 5582−5593.
(36) Mohamed, M. G.; El-Mahdy, A. F. M.; Kotp, M. G.; Kuo, S. W. Advances in porous organic polymers: Syntheses, structures, and diverse applications. *Mater. Adv.* **2022**, *3*, 707−733.
(37) Wang, T. X.; Liang, H. P.; Anito, D. A.; Ding, X.; Han, B. H. Emerging applications of porous organic polymers in visible-light photocatalysis. *J. Mater. Chem. A* **2020**, *8*, 7003−7034.
(38) Chen, L.; Chen, B.; Kang, J.; Yan, Z.; Jin, Y.; Yan, H.; Chen, S.; Xia, C. The synthesis of a novel conjugated microporous polymer and application on photocatalytic removal of uranium(VI) from wastewater under visible light. *Chem. Eng. J.* **2022**, *431*, 133222.
(39) Singh, P. N.; Mohamed, M. G.; Chaganti, S. V.; Sharma, S. U.; Ejaz, M.; Lee, J. T.; Kuo, S. W. Rational design of ultrastable conjugated microporous polymers based on pyrene and perylene units as high-performance organic electrode materials for supercapacitor applications. *ACS Appl. Energy Mater.* **2023**, *6*, 8277−8287.
(40) Sharma, S. U.; Elsayed, M. H.; Mekhemer, I. M. A.; Meng, T. S.; Chou, H. H.; Kuo, S. W.; Mohamed, M. G. Rational design of pyrene and thienyltriazine-based conjugated microporous polymers for high-performance energy storage and visible-light photocatalytic hydrogen evolution from water. *Giant* **2024**, *17*, 100217.
(41) Mohamed, M. G.; Chaganti, S. V.; Sharma, S. U.; Samy, M. M.; Ejaz, M.; Lee, J. T.; Zhang, K.; Kuo, S. W. Constructing conjugated microporous polymers containing the pyrene-4, 5, 9, 10-tetraone unit for energy storage. *ACS Appl. Energy Mater.* **2022**, *5*, 10130−10140.
(42) Lee, J. S. M.; Cooper, A. I. Advances in conjugated microporous polymers. *Chem. Rev.* **2020**, *120*, 2171−2214.
(43) Wang, S.; Zhang, C.; Shu, Y.; Jiang, S.; Xia, Q.; Chen, L.; Jin, S.; Hussain, I.; Cooper, A. I.; Tan, B. Layered microporous polymers by solvent knitting method. *Sci. Adv.* **2017**, *3*, 1602610.
(44) Mohamed, M. G.; Elsayed, M. H.; Elewa, A. M.; El-Mahdy, A. F. M.; Yang, C. H.; Mohammed, A. A. K.; Chou, H. H.; Kuo, S. W.

Pyrene-containing conjugated organic microporous polymers for photocatalytic hydrogen evolution from water. *Catal. Sci. Technol.* **2021**, *11*, 2229−2241.
(45) Côté, A. P.; Benin, A. I.; Ockwig, N. W.; O'Keeffe, M.; Matzger, A. J.; Yaghi, O. M. Porous, crystalline, covalent organic frameworks. *Science* **2005**, *310*, 1166−1170.
(46) Konstas, K.; Taylor, J. W.; Thornton, A. W.; Doherty, C. M.; Lim, W. X.; Bastow, T. J.; Df Kennedy, D. F.; Wood, C. D.; Cox, B. J.; Hill, J. M.; Hill, A. J.; Matthew, R.; Hill, M. R. Lithiated porous aromatic frameworks with exceptional gas storage capacity. *Angew. Chem., Int. Ed.* **2012**, *51*, 6639.
(47) Gao, X.; Shu, C.; Zhang, C.; Ma, W.; Ren, S. B.; Wang, F.; Chen, Y.; Zeng, J. H.; Jiang, J. X. Substituent effect of conjugated microporous polymers on the photocatalytic hydrogen evolution activity. *J. Mater. Chem. A* **2020**, *8*, 2404−2411.
(48) Mousa, A. O.; Lin, Z. I.; Chuang, C. H.; Chen, C. K.; Kuo, S. W.; Mohamed, M. G. Rational design of bifunctional microporous organic polymers containing anthracene and triphenylamine units for energy storage and biological applications. *Int. J. Mol. Sci.* **2023**, *24*, 8966.
(49) Mohamed, M. G.; Elsayed, M. H.; Li, C. J.; Hassan, A. E.; Mekhemer, I. M. A.; Musa, A. F.; Hussien, M. K.; Chen, L. C.; Chen, K. H.; Chou, H. H.; Kuo, S. W. Reticular design and alkyne bridge engineering in donor−π−acceptor type conjugated microporous polymers for boosting photocatalytic hydrogen evolution. *J. Mater. Chem. A* **2024**, *12*, 7693−7710.
(50) Chang, S. Y.; Elewa, A. M.; Mohamed, M. G.; Mekhemer, I. M. A.; Samy, M. M.; Zhang, K.; Chou, H. H.; Kuo, S. W. Rational design and synthesis of bifunctional Dibenzo [g,p] chrysene-based conjugated microporous polymers for energy storage and visible light-driven photocatalytic hydrogen evolution. *Mater. Today Chem.* **2023**, *33*, 101680.
(51) Byun, J.; Zhang, K. A. Designing conjugated porous polymers for visible light-driven photocatalytic chemical transformations. *Mater. Horiz.* **2020**, *7*, 15−31.
(52) Lee, J.-S. M.; Wu, T. H.; Alston, B. M.; Briggs, M. E.; Hasell, T.; Hu, C. C.; Cooper, A. I. Porosity-engineered carbons for supercapacitive energy storage using conjugated microporous polymer precursors. *J. Mater. Chem. A* **2016**, *4*, 7665−7673.
(53) Che, H.; Wang, J.; Wang, P.; Ao, Y.; Chen, J.; Gao, X.; Zhu, F.; Liu, B. Simultaneously Achieving Fast Intramolecular Charge Transfer and Mass Transport in Holey D−π−A Organic Conjugated Polymers for Highly Efficient Photocatalytic Pollutant Degradation. *JACS Au* **2023**, *3*, 1424−1434.
(54) Dong, X.; Zhao, H.; Zhang, K.; Lang, X. Pyrene-based porous organic materials for visible light photocatalysis. *Coord. Chem. Rev.* **2024**, *513*, 215902.
(55) Fu, M.; Zhang, C.; Chen, Y.; Fan, K.; Zhang, G.; Zou, J.; Gao, Y.; Dai, H.; Wang, X.; Wang, C. A thianthrene-based small molecule as a high-potential cathode for lithium−organic batteries. *Chem. Commun.* **2022**, *58*, 11993−11996.
(56) Etkind, S. I.; Lopez, J.; Zhu, Y. G.; Fang, J. H.; Ong, W. J.; Shao-Horn, Y.; Swager, T. M. Thianthrene-Based Bipolar Redox-Active Molecules Toward Symmetric All-Organic Batteries. *ACS Sustain. Chem. Eng.* **2022**, *10*, 11739−11750.
(57) Mohamed, M. G.; Hu, H. Y.; Santhoshkumar, S.; Madhu, M.; Mansoure, T. H.; Hsiao, C. W.; Ye, Y.; Huang, C. W.; Tseng, W. L.; Kuo, S. W. Design and Synthesis of Bifunctional Conjugated Microporous Polymers Containing Tetraphenylethene and Bisulfone Units for Energy Storage and Fluorescent Sensing of p-Nitrophenol. *Colloids Surf. A Physicochem. Eng. Asp.* **2024**, *680*, 132675.
(58) Mohamed, M. G.; Chang, S. Y.; Ejaz, M.; Samy, M. M.; Mousa, A. O.; Kuo, S. W. Design and synthesis of bisulfone-linked two-dimensional conjugated microporous polymers for CO_2 adsorption and energy storage. *Molecules* **2023**, *28*, 3234.
(59) Li, X. C.; Zhang, Y.; Wang, C. Y.; Wan, Y.; Lai, W.-Y.; Pang, H.; Huang, W. Redox-active triazatruxene-based conjugated microporous polymers for high-performance supercapacitors. *Chem. Sci.* **2017**, *8*, 2959−2965.
(60) Wang, H.; Liang, L.; Duan, L.; Sun, S.; Cheng, X. Fabrication of MWNT@CMPs and carbonized MWNT@CMPs for supercapacitors. *Mater. Chem. Phys.* **2019**, *226*, 309−317.
(61) Mohamed, M. G.; Hammad Elsayed, M.; Hassan, A. E.; Basit, A.; Mekhemer, I. M. A.; Chou, H. H.; Chen, K. H.; Kuo, S. W. Hybrid Porous Polymers Combination of Octavinylsilsesquioxane/Pyrene with Benzothiadiazole Units for Robust Energy Storage and Efficient Photocatalytic Hydrogen Production from Water. *ACS Appl. Polym. Mater.* **2024**, *6*, 5945−5956.
(62) Weng, T. H.; Mohamed, M. G.; Sharma, S. U.; Mekhemer, I. M. A.; Chou, H. H.; Kuo, S. W. Rationally Engineered Ultrastable Three-Dimensional (3D) Conjugated Microporous Polymers Containing Triptycene, Tetraphenylethene, and Benzothiadiazole Units as Exceptional High-Performance Organic Electrodes for Supercapacitors. *ACS Appl. Energy Mater.* **2023**, *6*, 9012−9024.
(63) Mohamed, M. G.; Chang, W. C.; Kuo, S. W. Crown Ether- and Benzoxazine-Linked Porous Organic Polymers Displaying Enhanced Metal Ion and CO_2 Capture through Solid State Chemical Transformation. *Macromolecules* **2022**, *55*, 7879−7892.
(64) Mohamed, M. G.; Chang, W. C.; Chaganti, S. V.; Sharma, S. U.; Lee, J. T.; Kuo, S. W. Dispersion of ultrastable crown-ether-functionalized triphenylamine and pyrene-linked porous organic conjugated polymers with single-walled carbon nanotubes as high-performance electrodes for supercapacitors. *Polym. Chem.* **2023**, *14*, 4589−4601.
(65) Mousa, A. O.; Lin, Z. I.; Chaganti, S. V.; Chuang, C. H.; Chen, C. K.; Kuo, S. W.; Mohamed, M. G. Bifunctional imidazolium linked tetraphenylethene based conjugated microporous polymers for dynamic antibacterial properties and supercapacitor electrodes. *Polym. Chem.* **2024**, *15*, 397−411.
(66) Shu, C.; Zhao, Y.; Zhang, C.; Gao, X.; Ma, W.; Ren, S. B.; Wang, F.; Chen, Y.; Zeng, J. H.; Jiang, J. X. Bisulfone-Functionalized Organic Polymer Photocatalysts for High-Performance Hydrogen Evolution. *ChemSusChem* **2020**, *13*, 369−375.
(67) Hu, D.; Jia, Y.; Yang, S.; Huang, F.; Dong, Y.; Du, P. Redox-active 2D porous organic polymers for high-performance supercapacitor. *J. Ind. Eng. Chem.* **2023**, *123*, 320−329.
(68) Mohamed, M. G.; Su, B. X.; Kuo, S. W. Robust Nitrogen-Doped Microporous Carbon via Crown Ether-Functionalized Benzoxazine-Linked Porous Organic Polymers for Enhanced CO_2 Adsorption and Supercapacitor Applications. *ACS Appl. Mater. Interfaces* **2024**, *16*, 40858−40872.
(69) Sandoval-Torrientes, R.; Zimmermann, I.; Calbo, J.; Aragó, J.; Santos, J.; Ortí, E.; Martín, N.; Nazeeruddin, M. K. Hole transporting materials based on benzodithiophene and dithienopyrrole cores for efficient perovskite solar cells. *J. Mater. Chem. A* **2018**, *6*, 5944−5951.
(70) Gao, J.; Zhao, J.; Wu, J.; Lei, Y.; Li, N.; Yu, J.; Sui, Z.; Wang, Y.; Yang, J.; Wang, Z. Preparation of highly conductive anion exchange membranes by introducing dibenzothiophene monomer into the polymer backbone. *J. Power Sources* **2024**, *602*, 234314.

https://doi.org/10.1021/acsapm.4c02368
ACS Appl. Polym. Mater. 2024, 6, 12247−12260